crystals

MDPI

Article

Global Instability of Rod Eutectic Growth in Directional Solidification

Yanlin Gan and Xiangming Li *

Faculty of Materials Science and Engineering, Kunming University of Science and Technology, Kunming 650093, China
* Correspondence: lixm@kust.edu.cn

Abstract: In our previous work, we obtained the uniformly valid asymptotic solution of a cylindrical rod eutectic. In order to further study the critical point of the stable growth of a rod eutectic, we have considered the unsteady growth of a rod eutectic on the basis of the steady solution of the rod eutectic. Based on the experimental system of rod eutectic growth, combined with solidification thermodynamics and kinetics, the unsteady mathematical model of the rod eutectic was established. We used the asymptotic analysis method to seek the analytical solution of the mathematical model and used the nonlinear stability analysis theory to analyze the analytical solution and establish the corresponding disturbance model. We obtained the analytic form of the global mode solution and the corresponding quantization conditions and find that there is a stable growth mode, namely the mode (ST-mode), for rod eutectic growth; when $\varepsilon < \varepsilon_{\mathrm{ST}}^{0}$, the rod eutectic growth is stable, when $\varepsilon > \varepsilon_{\mathrm{ST}}^{0}$, the rod eutectic growth is unstable and when $\varepsilon = \varepsilon_{\mathrm{ST}}^{0}$, the rod eutectic growth is of a neutral stability. The critical eutectic spacing of succinonitrile(D)camphor (SCN-DC) predicted by us is smaller than that predicted by Jackson–Hunt, which is consistent with the corresponding experimental data. Finally, we found that the critical eutectic spacing and stable region of rod eutectic growth changed little with the temperature gradient.

Keywords: directional solidification; rod eutectic growth; perturbation analysis; global steady (ST) mode

Citation: Gan, Y.; Li, X. Global Instability of Rod Eutectic Growth in Directional Solidification. *Crystals* **2023**, *13*, 548. https://doi.org/10.3390/cryst13030548

Academic Editors: Wolfram Miller, Jacek Krawczyk and Dariusz Szeliga

Received: 2 March 2023
Revised: 18 March 2023
Accepted: 20 March 2023
Published: 22 March 2023

1. Introduction

Eutectic growth is one of the important phenomena of solid–liquid interface morphology evolution in metal solidification systems. Therefore, the key problem of preparing eutectic materials is how to effectively control the solidification process of eutectic materials under given preparation conditions. In the process of eutectic solidification, there are two fundamental problems that are very important and which determine the quality and properties of the final product materials and that demand a lot of in-depth quantitative research to be conducted: the first is the thermodynamics of the eutectic solidification process; the second is the formation and evolution of the eutectic solid–liquid interface and the solid–solid interface. The two influence and interact with each other, forming an inseparable nonlinear dynamic system. The research focus of eutectic growth theory is to explore the coupling behavior of the two in eutectic growth. Therefore, the expected theoretical results of eutectic growth will make people have a deeper understanding of the formation of the eutectic microstructure, the evolution of the interface and the mechanism of microstructure stability.

The study of interface evolution, stability and selectivity in eutectic solidification systems has been one of the most important subjects in material science, condensed matter physics and nonlinear science [1–4]. Generally, regular eutectic mainly includes a lamellar eutectic and a rod eutectic. Most of the theories and experiments on eutectic growth are focused on the two-dimensional lamellar eutectic growth [1–19], while there are few reports on the three-dimensional rod eutectic [20–33]. For the growth of the three-dimensional rod eutectic, three-dimensional dimensions such as rod cross-sectional morphology (round, oval, peanut, etc.) and rod arrangement structure have important influences on the morphology of the eutectic. Therefore, it is of great theoretical significance to study the coupling behavior of the three-dimensional characteristic size, crystal growth kinetics and interface evolution in three-dimensional rod eutectic growth systems. Jackson and Hunt made important contributions to the theory of rod eutectic growth. They established a classical mathematical model for the growth of cylindrical rod eutectic and obtained the steady solution to cylindrical rod eutectic growth. Based on this, they used the average undercooling degree of the interface to correspond to the selection point of eutectic stable growth; as a result, the rod eutectic with eutectic spacing less than λ_m disappeared.

In 2007, Akamatsu et al. [24] observed the growth morphology of a SCN-DC rod eutectic in thin and thick sample containers in real time and showed that: (1) in thin sample containers, the minimum critical eutectic spacing of a periodic eutectic can grow stably at about 0.65 times that predicted with the Jackson–Hunt theory; when the eutectic spacing of the hypereutectic alloy during solidification growth is about 1.8 times that predicted with the Jackson–Hunt theory, the eutectic begins to grow in a double-period (the period is two eutectic spacing) oscillation mode. When the eutectic spacing in solidification growth of hypoeutectic alloy is about twice that predicted by Jackson–Hunt theory, the eutectic begins to grow in a single period (the period is one eutectic spacing) oscillation mode. (2) In the thick sample container, the eutectic has an irregular arrangement structure, and the average eutectic spacing is close to that predicted with the Jackson–Hunt theory, but the minimum eutectic spacing is still about 0.65 times of that predicted with the Jackson–Hunt theory. Subsequently, Serefoglu et al. [25,26] demonstrated the growth experiment of a SCN-DC rod eutectic and specifically studied the influence of container thickness on the arrangement of the rod eutectic. Recently, Perrut et al. [27] disturbed the eutectic growth system through the isothermal eutectic interface protruding to the liquid phase and observed the growth of the SCN-DC rod-like eutectic in real time for a long time. They found that the critical distance when the rod-like phase starts to split satisfies the scale relationship predicted with the Jackson–Hunt theory, and the eutectic distance is inversely proportional to the square root of solidification rate, while the critical distance when the rod-like phase starts to split is 1.2 times that predicted with the Jackson–Hunt theory. However, the critical eutectic spacing which begins to disappear does not meet the scale relationship predicted with the Jackson–Hunt theory, and with the decrease in the solidification rate, the critical eutectic spacing is farther and farther away from the critical eutectic spacing predicted with the Jackson–Hunt theory, that is, when the velocity decreases from 0.25 to 0.01 μm/s, the ratio of the two decreases from 0.96 times to 0.66 times. At the same time, when the critical eutectic spacing is close to the critical spacing predicted with the Jackson–Hunt theory, they also observed the spatial oscillation mode of rod eutectic growth. In 2021, Sabine Bottin-Rousseau et al. [34] observed the lamellar–rod transformation process of a directionally solidified eutectic alloy in real time for the first time. They found that at a low growth rate, the extended rod-like domain and lamellar domain coexisted for a long time, thus clearly proving the dynamic metastability between the energy band structure and the hexagonal structure in the non-equilibrium system. It is also found that the straight sheet is stable when it is in contact with the wall, and because it drifts along the inclined isotherm, the instability of its free-end varicose veins will become convective, which provides a laboratory example for how to produce a self-organized composite structure with a two-domain upper structure in solid. In 2022, M. Serefoglu et al. [35]. studied the lamellar–rod phase transformation process during eutectic growth by observing the directional solidification process of SCN-DC eutectic alloys with different thicknesses in real time and explored the coupling dynamics of eutectic growth with variable constraint effect. Morphology maps in terms of the solidification velocity V, interphase spacing λ and sample thickness δ were plotted. These maps permit locating the stability limits of rod-like and lamellar patterns as well as coexistence regions. Confinement in samples of intermediate thickness operates via a wall effect, which stabilizes and aligns the lamella ends, and a size effect, which can block some secondary instability modes prior to the lamellar breakup and the lamellar-to-rod transformation. In addition to observations showing mixed patterns and hysteresis behaviors, morphology maps in terms of the solidification velocity V, interphase spacing λ and sample thickness δ made evident the existence of a bistable domain of parameters. The rod elongation instability governs the rod-to-lamellar transformation. Complex spatiotemporal phenomena involving labyrinth, oscillatory and hybrid patterns were also reported, the multiscale dynamics of which are reminiscent of previous observations in directionally solidified eutectics [36]. The above experimental results show that in the eutectic growth system, the rod eutectic has a variety of stable growth morphology characteristics (cylindrical, elliptical, peanut, etc.); indeed, all kinds of rod eutectics have stable growth regions. In addition to the above stable morphology characteristics, there are also oscillation modes such as the single-cycle oscillation growth mode and double-cycle growth mode. To study the stability of rod eutectic growth is to reveal the mechanism of the rod eutectic growth of various morphology characteristics and determine the specific stable growth region; the study of the selectivity of rod eutectic growth is to analyze the transformation law of different eutectic growth modes and determine the critical transition region or critical point of various growth mode regions of the rod eutectic.

The stability and selectivity of rod eutectic growth cannot be completely solved with the Jackson–Hunt theory. Specifically, the main reason why the Jackson–Hunt theory failed to solve the problem of the selectivity of the minimum critical point for the stable growth of eutectic is that they made the following important assumptions in the process of solving: (1) the growth rate of the eutectic is sufficiently small, so that the effect of solidification rate on the diffusion effect of solute is ignored in the liquid solute diffusion equation. (2) The eutectic solid–liquid interface is a flat isothermal interface, which transforms the free boundary problem of the eutectic growth system into a simple boundary value problem. (3) The average undercooling degree at the interface between the α phase and the liquid phase is equal to the average undercooling degree at the interface between the β phase and the liquid phase, and the coupling effect of the morphology of the solid–liquid interface and the solubility of the interfacial solute is ignored. Since the eutectic interface (especially rod eutectic) is never a straight interface, and the problem is still a free boundary problem, the solid–liquid interface formed during eutectic growth is affected by the experimental conditions, and its specific morphology needs to be determined in the process of solving its mathematical model. Although some researchers [31–33] have perfected or modified the Jackson–Hunt theory, these theories have not solved the problem of the stability and selectivity of rod-like eutectic growth. This is mainly because none of these theories have obtained a globally consistent and effective analytical solution for rod eutectic growth systems.

Eutectic materials have special optical properties, magnetic properties, superconductivity, heat resistance and high strength. For example, a magnesium–lithium eutectic alloy has high rigidity, excellent electrical conductivity, impact resistance, super plasticity, creep resistance and corrosion resistance in addition to light weight [37–46]. Metal–gas eutectic materials not only have light weight, high stiffness and high impact energy absorption, but also have unique mechanical properties and thermal conductivity. In 2023, Naveed Hassan, Manickam Minakshi and Zhong-Tao Jiang et al. [37] systematically studied the thermophysical properties, thermal repeatability and thermal decomposition behavior of binary eutectic salt mixtures, and they found that 32 mol% LiCl-68 mol% was a potential candidate with a potential for thermal energy storage. This is because they found that the particles of 32 mol% LiCl-68 mol% were evenly distributed and dense and observed that the particle posture of the sample changed slightly before cycling, and the sample decomposed at 700○C, which further proved that the binary salt mixture had good morphology, uniform element distribution, good uniformity, good thermal performance and good thermal stability. So, to solve the stability problem of rod eutectic growth, it is necessary to explore the eutectic spacing of the rod-like eutectic growing steadily, as shown in Figure 1. In this paper, the linear instability mechanism of rod eutectic growth is studied by means of the interfacial wave (IFW) theory developed by Xu [47] in the 1990s. We performed the asymptotic analysis for the perturbations around the basic steady state of the rod eutectic system. We obtained the analytic form of the global mode solution and the corresponding quantization conditions and found that there was a stable growth mode, namely the ST mode (see Figure 1), for rod eutectic growth; when $\varepsilon < \varepsilon^0_{\mathrm{ST}}$, the rod eutectic growth is stable, when $\varepsilon > \varepsilon^0_{\mathrm{ST}}$, the rod eutectic growth is unstable and when $\varepsilon = \varepsilon^0_{\mathrm{ST}}$, the rod eutectic growth is of a neutral stability. The critical eutectic spacing of SCN-DC predicted by us is smaller than that predicted by J–H [25], which is consistent with the corresponding experimental data [25]. Finally, we found that the critical eutectic spacing and stable region of rod eutectic growth changed little with the temperature gradient.

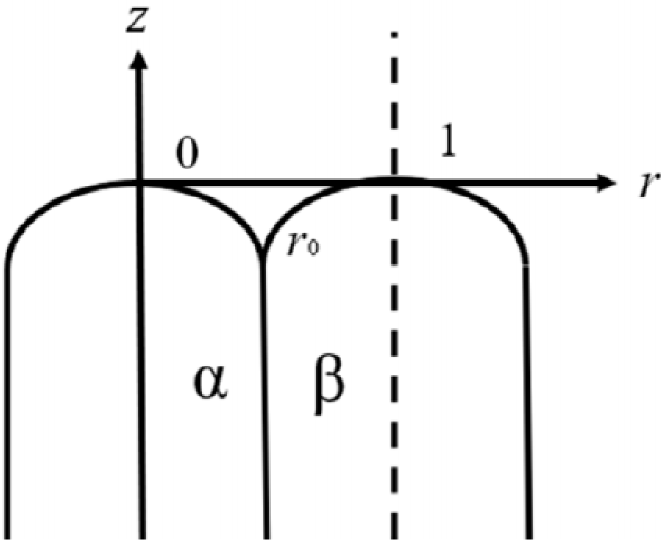

Figure 1. The geometry model of the metal–metal rod eutectic growth.

2. Mathematical Formulation of Rod Eutectic Growth

2.1. Unsteady Mathematical Model of Rod Eutectic Growth

Here, we consider the simple model of the growth of the axis-symmetric rod eutectics and present the non-dimensional form of the system for unsteady rod eutectic growth. We introduce the non-dimensional concentration field $C = (C_D - C_e)/(C_\beta - C_\alpha)$, where C_e is the eutectic concentration, C_D is the dimensional concentration in liquid phase, C_s is the equilibrium concentration of s-phase at eutectic temperature and subscripts $s = \alpha, \beta$ denote the two solid phases. Thus, the concentration field in the liquid phase subjects to the diffusion equation:

$$\frac{\partial^2 C}{\partial r^2} + \frac{1}{r}\frac{\partial C}{\partial r} + \frac{\partial^2 C}{\partial z^2} + \varepsilon\left(\frac{\partial C}{\partial z} - \frac{\partial C}{\partial t}\right) = 0, \quad (1)$$

where $\varepsilon = RV/\kappa_D$ is the Peclet number and κ_D is the solute diffusion coefficient in the liquid. Here, t is the time and the cylindrical coordinate system, (r, z), scaled as half the eutectic spacing R, moves with the freezing speed V in the z direction. Additionally, the dimensionless geometric model of the rod eutectic we used is shown in Figure 2:

Figure 1 shows the dimensionless cylindrical coordinate system selected by our group before, where the origin of the cylindrical coordinate system coincides with the vertex of the α phase, and r_0 represents the position where the α phase, β phase and liquid phase are combined, and the selected unit period is 1.

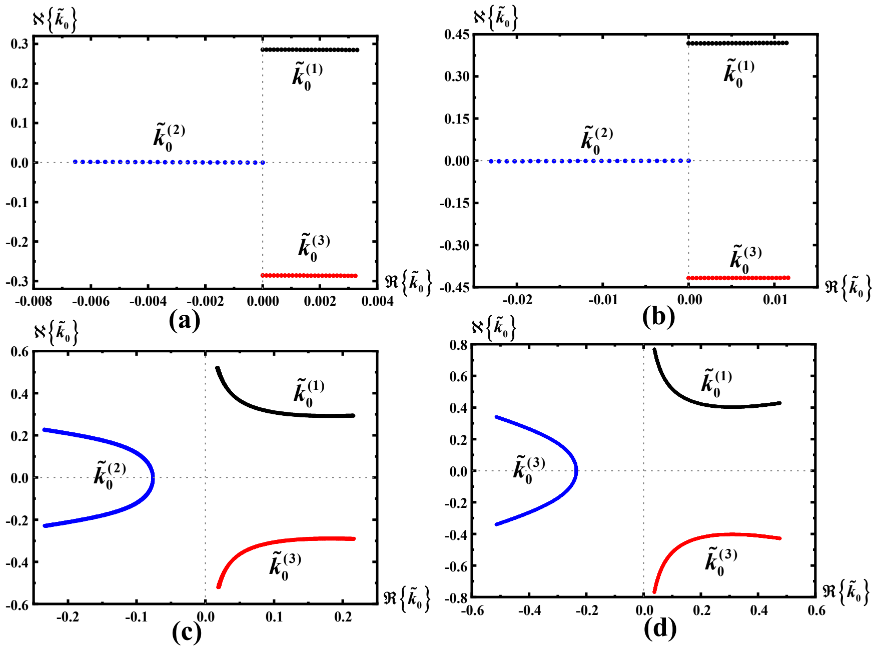

Figure 2. Figures showing the local dispersion relationship for typical cases of $\alpha - phase$ and $\beta - phase$, $(\Delta_s < 0)$ with $M_\alpha = 0.2$, $M_\beta = 0.25$, $\Lambda_\alpha = 2.2$, $\Lambda_\beta = 2.3$, $\theta_\alpha = 65^\circ$, $\theta_\beta = 50.55^\circ$, $C_\infty = 0.01$, $E_\alpha = 0.1388$, $E_\beta = -0.8599$. (**a**) Typical dispersion curves for the $\alpha - phase$, with the real eigenvalues $\sigma_0 = 0.0 \sim 0.1$. (**b**) Typical dispersion curves for the $\beta - phase$, with the real eigenvalues $\sigma_0 = 0.0 \sim 0.1$. (**c**) Typical dispersion curves for the $\alpha - phase$, with the complex eigenvalues $\sigma_0 = 0.2 + i\omega$, where $\omega = -0.1 \sim 0.1$. (**d**) Typical dispersion curves for the $\beta - phase$, with the complex eigenvalues $\sigma_0 = 0.2 + i\omega$, where $\omega = -0.1 - 0.1$. In the figures, the black line describes $\tilde{k}_0^{(1)}$, the red line describes $\tilde{k}_0^{(3)}$, the blue line describes $\tilde{k}_0^{(2)}$, $\Re\left\{\tilde{k}_0\right\}$ is the real part of $\tilde{k}_0$ and $\aleph\left\{\tilde{k}_0\right\}$ is the imaginary part of $\tilde{k}_0$.

At the liquid-solid interface $z = h_s(r)$, the Gibbs–Thomson condition is expressed as

$$\nu_s C = \frac{\varepsilon}{M_s}(z_* - h_s) + \frac{\Gamma_s}{\varepsilon}\frac{r h''_s(r) + \left(1 + (h'_s(r))^2\right)h'_s(r)}{r\left(1 + (h'_s(r))^2\right)^{3/2}}, \tag{2}$$

and the solute mass balance condition is written as

$$\varepsilon[(1 - \kappa_s)C + E_s]\left(\frac{\partial h_s}{\partial t} + 1\right) = -\frac{\partial C}{\partial z} + \frac{\partial h_s}{\partial r}\frac{\partial C}{\partial r}, \tag{3}$$

where z_* is the location of eutectic temperature, $v_\alpha = 1$, $v_\beta = -1$. The dimensionless parameters are denoted as following:

$$M_s = -\frac{\nu_s m_s V\left(C_\beta - C_\alpha\right)}{\kappa_D G},\ \Gamma_s = -\frac{\gamma_s T_e V}{\nu_s m_s L_s \kappa_D \left(C_\beta - C_\alpha\right)},\ E_s = \frac{C_e - C_s}{C_\beta - C_\alpha},$$

where m_s is the liquidus slope of the phase diagram, T_e is the eutectic temperature, L_s is the latent heat and γ_s is the interfacial tension among liquid–s phase interface.

At the triple phase junction, $r = r_0$, and the connection condition is

$$h_\alpha(r_0) = h_\beta(r_0) \tag{4}$$

and the slope of the liquid–solid interface is

$$h_s'(r_0) = -\nu_s \tan\theta_s, \tag{5}$$

where θ_s is the contact angle.

At infinity, as $z \to \infty$,

$$C \to C_\infty \tag{6}$$

where C_∞ is the solute concentration in the liquid phase far from the interface.

2.2. Steady Basic State of Rod Eutectic Growth

The above system provides a description of unsteady rod eutectic growth. When the time term is ignored, it is reduced to a steady state. The asymptotic solutions for the steady growth of rod eutectics have been obtained [33]. We summarize as follows for the solutions of the concentration, the liquid–solid interface and the triple phase junction:

$$\begin{cases} C_B(r,z) = C_\infty\left[1 - e^{-\varepsilon z} + \varepsilon d_1 e^{-\varepsilon z} + \frac{2\varepsilon}{C_\infty}\sum\limits_{n=1}^{\infty}\frac{J_1(\lambda_n r_0)J_0(\lambda_n r)}{\lambda_n{}^2 J_0{}^2(\lambda_n)}e^{-\lambda_n z} + o(\varepsilon)\right] \\ h_B(r) = \delta\left[-\frac{\tan\theta_s}{\sqrt{a_s}}\exp\left(v_s\sqrt{a_s}\,\bar{r}\right) + z_{*1} - v_s\bar{M}_s\left(d_1 + \sum_{n=1}^{\infty}\omega_n J_0(\lambda_n r)\right) + o(\delta)\right] \\ r_B = w_0 + o(\varepsilon) \end{cases}, \tag{7}$$

As $\varepsilon \to 0$, $\delta \to 0$, Equation (7) is uniformly valid, and we will analyze the instability mechanisms for Equation (7) by using the perturbation method. Additionally, for the specific expressions of parameters in Equation (7), please refer to the reference [33].

2.3. Linear Perturbed States of Rod Eutectic Growth

We now write the unsteady-state solutions in the following two parts:

$$\begin{cases} C(r,z,t,\varepsilon) = C_B(r,z,\varepsilon) + \widetilde{C}(r,z,t,\varepsilon) \\ h(r,t,\varepsilon) = h_B(r,\varepsilon) + \widetilde{h}(r,t,\varepsilon) \\ r_0(t,\varepsilon) = r_B(\varepsilon) + \widetilde{w}_0(t,\varepsilon) \end{cases} \tag{8}$$

Part I of the solution, $C_B(r,z,\varepsilon)$, $h_B(r,\varepsilon)$, $r_B(\varepsilon)$ are the basic steady-state solutions of the system. Part II of the unsteady perturbed states $\widetilde{C}(r,z,t,\varepsilon)$, $\widetilde{h}(r,t,\varepsilon)$ and $\widetilde{w}_0(t,\varepsilon)$ is considered as the small perturbations around the basic state. In the present paper, we assume that the eutectic spacing $2R$ is unperturbed, so that the parameter ε is time independent. However, when the concentration field is perturbed, the location of the triple point r_0 may be accordingly perturbed.

For the infinitesimal perturbations $\left|\widetilde{C}(r,z,t,\varepsilon)\right| \ll |C_B(r,z,\varepsilon)|$, $\left|\widetilde{h}(r,t,\varepsilon)\right| \ll |h_B(r,\varepsilon)|$, $\left|\widetilde{w}_0(t,\varepsilon)\right| \ll |r_B(\varepsilon)|$, one may derive the following linearized perturbed system:

$$\frac{\partial^2\widetilde{C}}{\partial r^2} + \frac{\partial\widetilde{C}}{\partial r}\frac{1}{r} + \frac{\partial^2\widetilde{C}}{\partial z^2} + \varepsilon\left(\frac{\partial\widetilde{C}}{\partial z} - \frac{\partial\widetilde{C}}{\partial t}\right) = 0 \tag{9}$$

With the boundary conditions:

1. As $z \to \infty$,

$$\widetilde{C} \sim 0 \tag{10}$$

2. As $r = 0$ or 1:

$$\widetilde{C} = \widetilde{h} = 0 \tag{11}$$

Here, we choose the cylindrical coordinate system to meet the requirement that the axis r=0 passes through the tip of the liquid—α interface, and $r = 1$ corresponds to half the eutectic spacing.

1. At the interface $z = h_B = \delta h_{s1} + \ldots \ll 1$, the interface conditions linearized at $z = 0$ can be written as follows:
    (1) the Gibbs–Thomson condition:

$$\nu_s\left(\tilde{C} + \frac{\partial C_B}{\partial z}\tilde{h}\right) = -\frac{\varepsilon}{M_s}\tilde{h} + \frac{\Gamma_s}{\varepsilon}\frac{r\tilde{h}''(r) + \tilde{h}'(r)}{r}, \tag{12}$$

    (2) the mass balance condition:

$$\varepsilon\left[(1-\kappa_s)\left(\tilde{C} + \frac{\partial C_B}{\partial z}\tilde{h}\right) + E_s\frac{\partial \tilde{h}}{\partial t}\right] = -\frac{\partial \tilde{C}}{\partial z} + h_{Br}\frac{\partial \tilde{C}}{\partial r} \tag{13}$$

2. At the triple phase junction, $r = r_0$, the connection condition for the perturbed interface is

$$\tilde{h}_\alpha(w_0) + \frac{\partial h_{s,\alpha}(w_0)}{\partial w_0}\tilde{w}_0 = \tilde{h}_\beta(w_0) + \frac{\partial h_{s,\beta}(w_0)}{\partial w_0}\tilde{w}_0, \tag{14}$$

and the connection condition of the perturbation interface derivative is

$$\left[\tilde{h}'_\alpha(w_0) + \frac{\partial^2 h_{s,\alpha}(w_0)}{\partial r^2}\tilde{w}_0\right] - \left(\frac{\cos\theta_\beta}{\cos\theta_\alpha}\right)^2\left[\tilde{h}'_\beta(w_0) + \frac{\partial^2 h_{s,\beta}(w_0)}{\partial r^2}\tilde{w}_0\right] = 0. \tag{15}$$

3. Multiple Variables Expansion Form of the Perturbed System

Here, it is presumed that the perturbed state involves multiple length scales, and we can use multivariate expansion method to solve the system. Therefore, we introduce the following variables [47]:

$$\begin{cases} t_+ = \frac{t}{\varepsilon_0} \\ r_+ = \frac{1}{\varepsilon_0}\int_{w_0}^{r}\tilde{k}_s(r_1, z)d\mathrm{r}_1 \, . \\ z_+ = \frac{1}{\varepsilon_0}\int_0^z \tilde{k}_s(r, z_1)dz_1 \end{cases} \tag{16}$$

where $\varepsilon_0 \ll 1$ and we will further express the perturbed states in the multiple variables form:

$$\tilde{C}(r,z,t,\varepsilon_0) = \overset{\sim}{\mathbb{C}}(r,z,r_+,z_+,t_+,\varepsilon_0),\ \tilde{h}(r,t,\varepsilon_0) = \overset{\sim}{\mathbb{H}}(r,r_+,t_+,\varepsilon_0). \tag{17}$$

3.1. The System with Multiple Variables

It is derived that

$$\tilde{k}^2\left(\frac{\partial^2}{\partial {r_+}^2} + \frac{\partial^2}{\partial {z_+}^2}\right)\overset{\sim}{\mathbb{C}} = 0. \tag{18}$$

with the boundary conditions:

1. As $z_+ \to \infty$,

$$\overset{\sim}{\mathbb{C}} \sim 0, \tag{19}$$

2. As $r_+ = 0$ or 1:

$$\overset{\sim}{\mathbb{C}} = \overset{\sim}{\mathbb{H}} = 0. \tag{20}$$

3. The interface $z = z_+ = 0$, and we have

I. the Gibbs–Thomson condition:

$$\nu_s\left[\widetilde{\mathbb{C}}+\varepsilon C_\infty\left(1-\sum_{n=1}^{\infty}\omega_n\lambda_n J_0(\lambda_n r)\right)\widetilde{\mathbb{H}}\right]=-\frac{\varepsilon}{M_s}\widetilde{\mathbb{H}}+\frac{{\Lambda_s}^2\delta^2\varepsilon}{M_s}\frac{\widetilde{k}^2}{{\varepsilon_0}^2}\frac{d^2\widetilde{\mathbb{H}}}{{dr_+}^2}+O(\varepsilon). \quad (21)$$

Here, Λ_s is an undetermined parameter, which needs to be determined by using boundary conditions and connection conditions, and its specific value varies with the growth conditions of eutectic.

II. the mass balance condition:

$$\widetilde{k}\frac{\partial\widetilde{\mathbb{C}}}{\partial z_+}-h_{Br}\widetilde{k}\frac{\partial\widetilde{\mathbb{C}}}{\partial r_+}+\varepsilon E_s\frac{\partial\widetilde{\mathbb{H}}}{\partial t_+}=0. \quad (22)$$

One may expend the perturbed states in the following asymptotic form in the limits $\varepsilon\to 0$, $\varepsilon_0\to 0$:

$$\begin{cases}\widetilde{\mathbb{C}}(r,z,r_+,z_+,t_+,\varepsilon_0,\varepsilon)=\varepsilon\left(\widetilde{\mathbb{C}}_0(r,z,r_+,z_+)+q(\varepsilon,\varepsilon_0)\widetilde{\mathbb{C}}_1(r,z,r_+,z_+)+\ldots\right)e^{\sigma t_+}\\ \widetilde{\mathbb{H}}(r,r_+,t_+,\varepsilon_0,\varepsilon)=\left(\widetilde{\mathbb{H}}_0(r,r_+)+q(\varepsilon,\varepsilon_0)\widetilde{\mathbb{H}}_1(r,r_+)+\ldots\right)e^{\sigma t_+}\\ \widetilde{r}_0(t_+,\varepsilon_0,\varepsilon)=\left(\widetilde{w}_0+q(\varepsilon,\varepsilon_0)\widetilde{w}_1+\ldots\right)e^{\sigma t_+}\end{cases}, \quad (23)$$

where $q(\varepsilon,\varepsilon_0)\ll 1$.

According to the above system, we will also set

$$\begin{cases}\widetilde{k}(r,z,\varepsilon_0,\varepsilon)=\widetilde{k}_0(r,z)+q(\varepsilon,\varepsilon_0)\widetilde{k}_1(r,z)+\cdots\\ \sigma(\varepsilon_0,\varepsilon)=\sigma_0(\varepsilon_0)+q(\varepsilon,\varepsilon_0)\sigma_1(\varepsilon_0)+\cdots\end{cases}, \quad (24)$$

3.2. Leading Order Approximate System

From the converted MV form of the system, by neglecting all the higher order small terms one may derive the following leading order approximate system, and in order to ensure the balance between the two sides of Equations (21) and (22), we must set $\varepsilon_0=\delta$.

It is derived that

$$\left(\frac{\partial^2}{\partial {r_+}^2}+\frac{\partial^2}{\partial {z_+}^2}\right)\widetilde{\mathbb{C}}_0=0, \quad (25)$$

with the following boundary conditions:

1. As $z\to\infty$,

$$\widetilde{\mathbb{C}}_0\sim 0. \quad (26)$$

2. At the tips of the solid phases: r= 0 or 1:

$$\widetilde{\mathbb{C}}_0=\widetilde{\mathbb{H}}_0=0. \quad (27)$$

3. At the interface, letting $z=0$, we have

   (1). the Gibbs–Thomson condition:

$$\nu_s\left[\widetilde{\mathbb{C}}_0+C_\infty\left(1-\sum_{n=1}^{\infty}\omega_n\lambda_n J_0(\lambda_n r)\right)\widetilde{\mathbb{H}}_0\right]=-\frac{\widetilde{\mathbb{H}}_0}{M_s}+\frac{{\Lambda_s}^2{\widetilde{k}_0}^{\,2}}{M_s}\frac{d^2\widetilde{\mathbb{H}}_0}{{dr_+}^2}, \quad (28)$$

   (2). The mass balance condition:

$$\widetilde{k}_0\frac{\partial\widetilde{\mathbb{C}}_0}{\partial z_+}-h_{Br}\widetilde{k}_0\frac{\partial\widetilde{\mathbb{C}}_0}{\partial r_+}+E_s\widetilde{\mathbb{H}}_0\sigma_0=0, \quad (29)$$

(3). The connection conditions at the triple junction $r = w_0$ as follows:

$$\widetilde{\mathbb{H}}_{0,\alpha}(w_0) = \widetilde{\mathbb{H}}_{0,\beta}(w_0);\ \widetilde{k}_{0,\alpha}\frac{\partial\widetilde{\mathbb{H}}_{0,\alpha}}{\partial r_+} = \widetilde{k}_{0,\beta}\left(\frac{\cos\theta_\beta}{\cos\theta_\alpha}\right)^2\frac{\partial\widetilde{\mathbb{H}}_{0,\beta}}{\partial r_+}. \tag{30}$$

We can solve the above system and obtain the analytical solution of the above system. We can consider the complex solutions for the concentration field as $\widetilde{\mathbb{C}}_0(\varsigma) = \widetilde{\mathbb{C}}_0(r_+ + \mathrm{i}z_+)$, where $\widetilde{\mathbb{C}}_0(\varsigma)$ is an analytic periodic function of $\varsigma = (r_+ + \mathrm{i}z_+)$ and subjects to the far field condition: $z \to \infty$, $\widetilde{\mathbb{C}}_0 \to 0$. We deduce that

$$\widetilde{\mathbb{C}}_0(\varsigma) = \textstyle\sum_{n=0}^{\infty} \widetilde{d}_n \mathrm{e}^{\mathrm{i}n\pi\varsigma}, \tag{31}$$

Then, from the interface conditions, one may derive the normal mode solution for the interface shape as $\widetilde{\mathbb{H}}_0(r) = \widetilde{D}_0\mathrm{e}^{\mathrm{i}r_+}$, where $\widetilde{D}_0$ is a piece-wise constant to be determined, which has different values in the different sub-intervals $(0 < r < w_0)$ and $(w_0 < r < 1)$.

From the above, we can derive the following dispersion relationship:

$$\sigma_0 = Q_0(r)\widetilde{k}_0\left[-\Lambda_s{}^2\widetilde{k}_0{}^2 - v_s C_\infty M_s + 2M_s v_s\sum_{n=1}^{\infty}\frac{J_0(\lambda_n r)J_1(\lambda_n r_0)}{\lambda_n J_0{}^2(\lambda_n)} - 1\right], \tag{32}$$

where $Q_0(r) = [1 + \mathrm{i}h_{Br}]/v_s M_s E_s$, and

$$\Delta_s = -v_s C_\infty M_s + 2v_s M_s\textstyle\sum_{n=1}^{\infty}\displaystyle\frac{J_0(\lambda_n r)J_1(\lambda_n r_0)}{\lambda_n J_0{}^2(\lambda_n)} - 1. \tag{33}$$

Based on the above Equation (32), we can give three roots about $\tilde{k}_0^{(i)}(r), (i = 1, 2, 3)$

4. According to the expression of σ_0, we can discuss it in the following three cases:

(1). For the case $\Delta_s < 0$, for the $\alpha - phase$ and $\beta - phase$, M and N will be imaginary numbers; from Equation (32), we deduce that

$$\begin{cases} \tilde{k}_0^{(1)}(r) = M\cos\left[\frac{1}{3}arccos\left(\frac{\sigma_0}{NQ_0(r)}\right)\right] \\ \tilde{k}_0^{(2)}(r) = M\cos\left[\frac{1}{3}arccos\left(\frac{\sigma_0}{NQ_0(r)}\right) + \frac{4}{3}\pi\right], \\ \tilde{k}_0^{(3)}(r) = M\cos\left[\frac{1}{3}arccos\left(\frac{\sigma_0}{NQ_0(r)}\right) + \frac{2}{3}\pi\right] \end{cases} \tag{34}$$

where $M = \left(4\Delta_s/3\Lambda_s{}^2\right)^{\frac{1}{2}}$, $N = -\left(4/27\Lambda_s{}^2\right)^{\frac{1}{2}}\Delta_s{}^{\frac{3}{2}}$, and we assign the values to the parameters in Equation (34) and obtain Figure 2:

(2). As $\Delta_s = 0$, Equation (32) cannot be applied in this case, in which case $\tilde{k}_0^{(1)} = \tilde{k}_0^{(2)} = \tilde{k}_0^{(3)} = 0$ and $M = N = 0$.

(3). For the case $\Delta_s > 0$, for the $\alpha - phase$ and $\beta - phase$, M and N will be real numbers; from Equation (32), we deduce that

$$\begin{cases} \tilde{k}_0^{(1)}(r) = M\cos\left[\frac{1}{3}arccos\left(\frac{\sigma_0}{NQ_0(r)}\right)\right] \\ \tilde{k}_0^{(2)}(r) = M\cos\left[\frac{1}{3}arccos\left(\frac{\sigma_0}{NQ_0(r)}\right) + \frac{2}{3}\pi\right], \\ \tilde{k}_0^{(3)}(r) = M\cos\left[\frac{1}{3}arccos\left(\frac{\sigma_0}{NQ_0(r)}\right) + \frac{4}{3}\pi\right] \end{cases} \tag{35}$$

where $M=\left(4\Delta_s/3\Lambda_s{}^2\right)^{\frac{1}{2}}$, $N=-\left(4/27\Lambda_s{}^2\right)^{\frac{1}{2}}\Delta_s{}^{\frac{3}{2}}$, and we assign the values to the parameters in Equation (35) and obtain Figure 3:

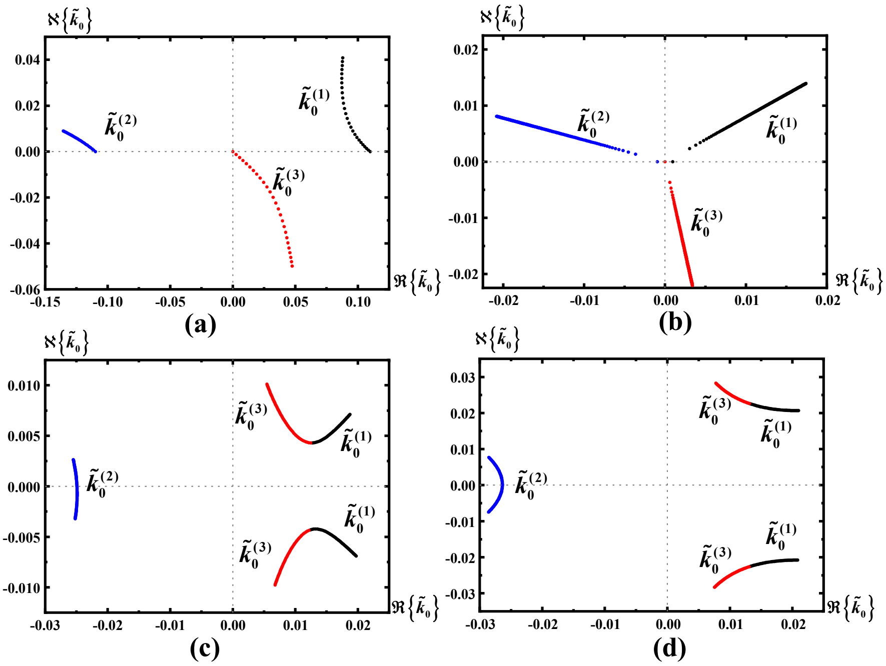

Figure 3. Figures showing the local dispersion relationship for typical cases of $\alpha-phase$ and $\beta-phase$, $(\Delta_s>0)$ with $M_\alpha=0.35$, $M_\beta=3.3$, $\Lambda_\alpha=2.2$, $\Lambda_\beta=2.3$,$\theta_\alpha=65^\circ$, $\theta_\beta=50.55^\circ$, $C_\infty=0.01$, $E_\alpha=0.1388$, $E_\beta=-0.8599$. (**a**) Typical dispersion curves for the $\alpha-phase$, with the real eigenvalues $\sigma_0=0.0\sim0.1$. (**b**) Typical dispersion curves for the $\beta-phase$, with the real eigenvalues $\sigma_0=0.0\sim0.1$. (**c**) Typical dispersion curves for the $\alpha-phase$, with the complex eigenvalues $\sigma_0=0.2+\mathrm{i}\omega$, where $\omega=-0.1\sim0.1$. (**d**) Typical dispersion curves for the $\beta-$ interface, with the complex eigenvalues $\sigma_0=0.2+\mathrm{i}\omega$, where $\omega=-0.1\sim0.1$. In the figures, the black line describes $\overset{\sim(1)}{k}_0$, the red line describes $\overset{\sim(3)}{k}_0$, the blue line describes $\overset{\sim(2)}{k}_0$, $\Re\left\{\tilde{k}_0\right\}$ is the real part of $\tilde{k}_0$ and $\aleph\left\{\tilde{k}_0\right\}$ is the imaginary part of $\tilde{k}_0$.

For a given σ_0, from Equation (32), we can obtain three roots as the function of σ_0, $\left\{\overset{\sim(1)}{k}_0,\overset{\sim(2)}{k}_0,\overset{\sim(3)}{k}_0\right\}$ as shown in Figures 2 and 3, and from Figures 2 and 3, we find out $\Re\left\{\overset{\sim(1)}{k}_0\right\}\geq\Re\left\{\overset{\sim(3)}{k}_0\right\}>0>\Re\left\{\overset{\sim(2)}{k}_0\right\}$. So, in viewing the form of Equation (31), to have a finite concentration field as $z\to\infty$, the fundamental solution corresponding to $\left\{\overset{\sim(2)}{k}_0\right\}$ must be ruled out. As a consequence, the perturbed state solutions can be expressed as

$$\overset{\sim}{\mathbb{H}}_{0,s}(r)=\begin{cases}\overset{\sim(1)}{D}_{0,\alpha}\mathrm{e}^{\frac{\mathrm{i}}{\varepsilon_0}\int_{w_0}^{r}\overset{\sim(1)}{k}_{0,\alpha}(r_1)\mathrm{d}r_1}+\overset{\sim(3)}{D}_{0,\alpha}\mathrm{e}^{\frac{\mathrm{i}}{\varepsilon_0}\int_{w_0}^{r}\overset{\sim(3)}{k}_{0,\alpha}(r_1)\mathrm{d}r_1},(0<r<w_0)\\ \overset{\sim(1)}{D}_{0,\beta}\mathrm{e}^{\frac{\mathrm{i}}{\varepsilon_0}\int_{w_0}^{r}\overset{\sim(1)}{k}_{0,\beta}(r_1)\mathrm{d}r_1}+\overset{\sim(3)}{D}_{0,\beta}\mathrm{e}^{\frac{\mathrm{i}}{\varepsilon_0}\int_{w_0}^{r}\overset{\sim(3)}{k}_{0,\beta}(r_1)\mathrm{d}r_1},(w_0<r<1)\end{cases}. \tag{36}$$

In what follows, we shall give the solutions in different subintervals separately.

4. Perturbed State Solutions in the Subinterval and Quantization Condition

To derive the global modes of the system, we need to apply the connection conditions $\overset{\sim}{\mathbb{H}}_{0,\alpha}(0)=0$ at the triple phase junction.

We apply the tip condition: $\overset{\sim}{\mathbb{H}}_{0,\alpha}(0) = 0$, $\overset{\sim}{\mathbb{H}}_{0,\beta}(1) = 0$. It is obtained that

$$\overset{\sim}{\mathbb{H}}_{0,\alpha}(0) = \tilde{D}^{(1)}_{0,\alpha} \mathrm{e}^{\frac{\mathrm{i}}{\varepsilon_0}\int_{w_0}^{0} \tilde{k}^{(1)}_{0,\alpha}(r_1)\mathrm{d}r_1} + \tilde{D}^{(3)}_{0,\alpha} \mathrm{e}^{\frac{\mathrm{i}}{\varepsilon_0}\int_{w_0}^{0} \tilde{k}^{(3)}_{0,\alpha}(r_1)\mathrm{d}r_1} = 0. \tag{37}$$

$$\overset{\sim}{\mathbb{H}}_{0,\beta}(1) = \tilde{D}^{(1)}_{0,\beta} \mathrm{e}^{\frac{\mathrm{i}}{\varepsilon_0}\int_{w_0}^{1} \tilde{k}^{(1)}_{0,\beta}(r_1)\mathrm{d}r_1} + \tilde{D}^{(3)}_{0,\beta} \mathrm{e}^{\frac{\mathrm{i}}{\varepsilon_0}\int_{w_0}^{1} \tilde{k}^{(3)}_{0,\beta}(r_1)\mathrm{d}r_1} = 0. \tag{38}$$

Thus, one may write the solution in the subinterval ($0 < r < w_0$) as

$$\overset{\sim}{\mathbb{H}}_{0,\alpha}(r) = \tilde{D}^{(1)}_{0,\alpha} \left[\tilde{H}_{1,\alpha}(r) - \mathrm{e}^{-\mathrm{i}\chi_\alpha} \tilde{H}_{3,\alpha}(r) \right], \tag{39}$$

where we have set

$$\tilde{H}_{1,\alpha}(r) = \mathrm{e}^{\frac{\mathrm{i}}{\varepsilon_0}\int_{w_0}^{0} \tilde{k}^{(1)}_{0,\alpha}(r_1)\mathrm{d}r_1},$$
$$\tilde{H}_{3,\alpha}(r) = \mathrm{e}^{\frac{\mathrm{i}}{\varepsilon_0}\int_{w_0}^{0} \tilde{k}^{(3)}_{0,\alpha}(r_1)\mathrm{d}r_1}$$

and

$$\chi_\alpha = \frac{1}{\varepsilon_0}\int_0^{w_0} \left[\tilde{k}^{(1)}_{0,\alpha}(r_1) - \tilde{k}^{(3)}_{0,\alpha}(r_1) \right] \mathrm{d}r_1 \tag{40}$$

Additionally, in the subinterval ($w_0 < r < 1$), given as

$$\overset{\sim}{\mathbb{H}}_{0,\beta}(r) = \tilde{D}^{(1)}_{0,\beta} \left[\tilde{H}_{1,\beta}(r) - \mathrm{e}^{-\mathrm{i}\chi_\beta} \tilde{H}_{3,\beta}(r) \right], \tag{41}$$

where we have set

$$\tilde{H}_{1,\beta}(r) = \mathrm{e}^{\frac{\mathrm{i}}{\varepsilon_0}\int_{w_0}^{1} \tilde{k}^{(1)}_{0,\beta}(r_1)\mathrm{d}r_1},$$
$$\tilde{H}_{3,\beta}(r) = \mathrm{e}^{\frac{\mathrm{i}}{\varepsilon_0}\int_{w_0}^{1} \tilde{k}^{(3)}_{0,\beta}(r_1)\mathrm{d}r_1}$$

and defined

$$\chi_\beta = -\frac{1}{\varepsilon_0}\int_{w_0}^{1} \left[\tilde{k}^{(1)}_{0,\beta}(r_1) - \tilde{k}^{(3)}_{0,\beta}(r_1) \right] \mathrm{d}r_1 \tag{42}$$

Here, $\tilde{D}^{(1)}_{0,\alpha}$ and $\tilde{D}^{(1)}_{0,\beta}$ can be any real numbers, but we need to determine the proportionality between them, so we now apply the connection conditions at the triple phase junction ($r = w_0$)

The condition $\overset{\sim}{\mathbb{H}}_{0,\alpha}(w_0^-) = \overset{\sim}{\mathbb{H}}_{0,\beta}(w_0^+)$ yields that

$$\tilde{D}^{(1)}_{0,\alpha}\left[1 - \mathrm{e}^{-\mathrm{i}\chi_\alpha}\right] = \tilde{D}^{(1)}_{0,\beta}\left[1 - \mathrm{e}^{-\mathrm{i}\chi_\beta}\right] \tag{43}$$

The condition $\tilde{k}_{0,\alpha}\frac{\partial \tilde{H}_{0,\alpha}}{\partial r_+} = \tilde{k}_{0,\beta}\left(\frac{\cos\theta_\beta}{\cos\theta_\alpha}\right)^2 \frac{\partial \tilde{H}_{0,\beta}}{\partial r_+}$ yields that

$$\begin{aligned} &\tilde{D}^{(1)}_{0,\alpha}\left[\tilde{k}^{(1)}_{0,\alpha}(w_0^-) - \mathrm{e}^{-\mathrm{i}\chi_\alpha} \frac{\tilde{k}^{(1)}_{0,\alpha}(0)\tilde{k}^{(3)}_{0,\alpha}(w_0^-)}{\tilde{k}^{(3)}_{0,\alpha}(0)} \right] \\ &= \left(\frac{\cos\theta_\beta}{\cos\theta_\alpha}\right)^2 \tilde{D}^{(1)}_{0,\beta}\left[\tilde{k}^{(1)}_{0,\beta}(w_0^+) - \mathrm{e}^{-\mathrm{i}\chi_\beta}\tilde{k}^{(3)}_{0,\beta}(w_0^+) \right] \end{aligned} \tag{44}$$

By combining Equations (43) and (44), we obtain the following quantization condition:

$$\frac{\left[1-\mathrm{e}^{-\mathrm{i}\chi_\alpha}\right]}{\left[1-\mathrm{e}^{-\mathrm{i}\chi_\beta}\right]} = \left(\frac{\cos\theta_\beta}{\cos\theta_\alpha}\right)^2 \frac{\left[\overset{\sim(1)}{k}_{0,\alpha}(w_0^-) - \mathrm{e}^{-\mathrm{i}\chi_\alpha}\overset{\sim(3)}{k}_{0,\alpha}(w_0^-)\right]}{\left[\overset{\sim(1)}{k}_{0,\beta}(w_0^+) - \mathrm{e}^{-\mathrm{i}\chi_\beta}\overset{\sim(3)}{k}_{0,\beta}(w_0^+)\right]} \tag{45}$$

From the above quantization condition, one can calculate the eigenvalues $\sigma_0 = \sigma_0(\varepsilon_0)$ as a function of ε_0 and other physical parameters.

5. The Global Steady (ST) Mode of Perturbed States

We find that the system allows a set of steady perturbed state mode. To do so, let $\sigma_0 = 0$ in the quantization condition. Thus, from the quantization condition one can solve for some critical values of the real pattern parameters $\varepsilon = \varepsilon_{\mathrm{ST}}$ with given growth conditions V, G and C_∞. The steady mode is used as the ST mode.

We first solve the wave number functions of the ST modes from the local dispersion Equation (32), which is as follows

$$Q_0(r)\tilde{k}_0\left[-\Lambda_{\mathrm{s}}{}^2\tilde{k}_0{}^2 - C_\infty M_s v_s + 2M_s v_s \textstyle\sum_{n=1}^{\infty} \displaystyle\frac{J_0(\lambda_n r)J_1(\lambda_n r_0)}{\lambda_n J_0{}^2(\lambda_n)} - 1\right] = 0. \tag{46}$$

From Equation (46) we can obtain the following situations:

$$(1)\begin{cases} \overset{\sim(1)}{k}_0 = \sqrt{\frac{\Delta_{\mathrm{s}}}{\Lambda_{\mathrm{s}}{}^2}} \\ \overset{\sim(3)}{k}_0 = 0 \end{cases}, (\Delta_s > 0);\ (2)\begin{cases} \overset{\sim(1)}{k}_0 = \frac{(-\Delta_{\mathrm{s}})^{\frac{1}{2}}\mathrm{i}}{\Lambda_{\mathrm{s}}} \\ \overset{\sim(3)}{k}_0 = \frac{-(-\Delta_{\mathrm{s}})^{\frac{1}{2}}\mathrm{i}}{\Lambda_{\mathrm{s}}} \end{cases}, (\Delta_s < 0). \tag{47}$$

As $\Delta_s < 0$, here we set

$$X = \frac{2}{\varepsilon_0}\left|\overset{\sim(1)}{k}_{0,\alpha}(w_0^-)\right| w_0,\ \mathbb{A}_1 = \left(\frac{\cos\theta_\beta}{\cos\theta_\alpha}\right)^2 \frac{\overset{\sim(1)}{k}_{0,\alpha}}{\overset{\sim(1)}{k}_{0,\beta}},\ \mathbb{B} = \frac{\overset{\sim(1)}{k}_{0,\beta}(1-w_0)}{\overset{\sim(1)}{k}_{0,\alpha} w_0}.$$

From Equation (45), we obtain:

$$\frac{\left[1-\mathrm{e}^{X}\right]}{\left[1-\mathrm{e}^{-\mathbb{B}X}\right]} = \mathbb{A}_1 \frac{\left[1+\mathrm{e}^{X}\right]}{\left[1+\mathrm{e}^{-\mathbb{B}X}\right]}, \tag{48}$$

since $X > 0$, $\mathbb{B} > 0$, $\mathbb{A}_1 > 0$, $1-\exp(X) < 0$, $1+\exp(X) > 0$, $1-\exp(-\mathbb{B}X) > 0$, $1+\exp(-\mathbb{B}X) > 0$, Equation (48) is not valid, so we will focus on $\Delta_s > 0$.

As $\Delta_s > 0$, we can obtain that from Equations (40) and (42):

$$\chi_\alpha = \frac{1}{\varepsilon_0}\int_0^{w_0}\left[\overset{\sim(1)}{k}_{0,\alpha}(r_1) - \overset{\sim(3)}{k}_{0,\alpha}(r_1)\right]\mathrm{d}r_1 \approx \frac{1}{\varepsilon_0}\overset{\sim(1)}{k}_{0,\alpha}(w_0^-)w_0, \tag{49}$$

$$\chi_\beta = -\frac{1}{\varepsilon_0}\int_{w_0}^{1}\left[\overset{\sim(1)}{k}_{0,\beta}(r_1) - \overset{\sim(3)}{k}_{0,\beta}(r_1)\right]\mathrm{d}r_1 \approx -\frac{1}{\varepsilon_0}\overset{\sim(1)}{k}_{0,\beta}(w_0^+)(1-w_0) = \frac{-\overset{\sim(1)}{k}_{0,\beta}(w_0^+)(1-w_0)}{\overset{\sim(1)}{k}_{0,\alpha} w_0}\chi_\alpha, \tag{50}$$

here, we set

$$X_1 = \frac{1}{\varepsilon_0}\overset{\sim(1)}{k}_{0,\alpha}(w_0^-)w_0,\ \mathbb{A}_1 = \left(\frac{\cos\theta_\beta}{\cos\theta_\alpha}\right)^2 \frac{\overset{\sim(1)}{k}_{0,\alpha}}{\overset{\sim(1)}{k}_{0,\beta}},\ \mathbb{B} = \frac{\overset{\sim(1)}{\mathrm{k}}_{0,\beta}(1-w_0)}{\overset{\sim(1)}{k}_{0,\alpha}w_0},$$

the variable X_1 is related to the parameter ε, $\mathbb{A}_1$ is related to the growth parameter G and V, which measures the effect of the triple point, and $\mathbb{B}$ is a constant determined by the thermodynamic properties of the system and the growth parameter G and V. As $\sigma_0 = 0$, from Equation (45) we can obtain the following solution:

$$\varepsilon_{\mathrm{ST}}^n = \frac{\sqrt{M_\alpha\Gamma_\alpha}X_1{}_{(n)}^*}{\left(-C_\infty M_\alpha v_\alpha + 2M_\alpha v_\alpha \sum_{n=1}^{\infty}\frac{J_0(\lambda_n w_0^-)J_1(\lambda_n w_0)}{\lambda_n {J_0}^2(\lambda_n)} - 1\right)^{\frac{1}{2}} w_0}, (n = 0, 1\cdots). \tag{51}$$

From Equation (51), we can know the positive correlation between $\varepsilon_{\mathrm{ST}}^n$ and $X_1{}_{(n)}^*$, so we can obtain a group of relations about $\varepsilon_{\mathrm{ST}}^n$: $\left(\varepsilon_{\mathrm{ST}}^0 < \varepsilon_{\mathrm{ST}}^1 < \varepsilon_{\mathrm{ST}}^2 < \cdots\right)$; it can also be seen from Equation (32) that the real part of σ_0 is positively related to ε_0 [1], so that we think when $\varepsilon < \varepsilon_{\mathrm{ST}}^0$, the rod eutectic growth is stable; therefore, $\varepsilon_{\mathrm{ST}}^0$ corresponds to the minimum critical point of rod eutectic growth. After a lot of calculation with the experimental data [25], from Equation (51) we can obtain the relationship between $\varepsilon_{\mathrm{ST}}^n$ and V, as shown in Figure 4:

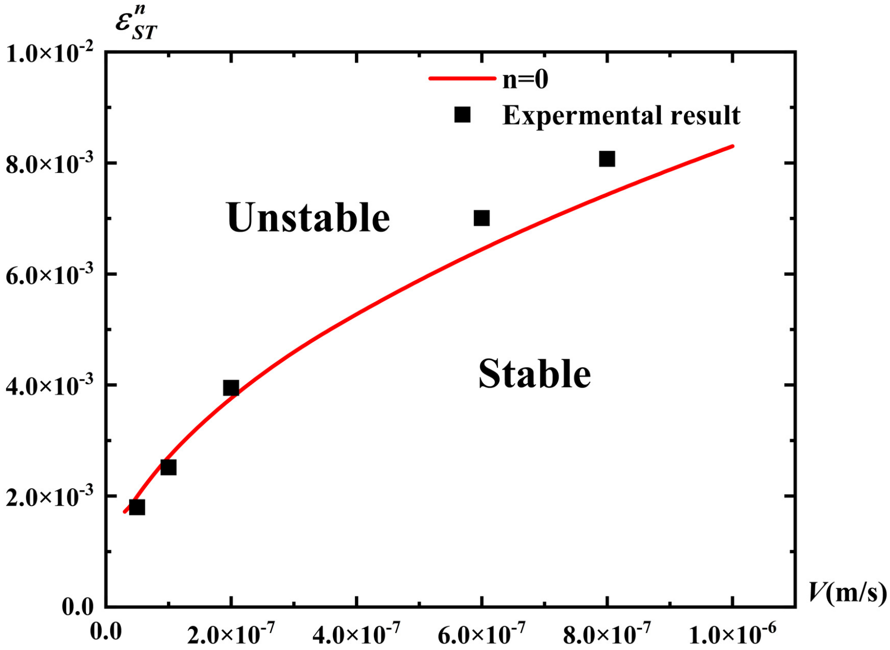

Figure 4. The curve of the critical numbers of $\varepsilon_{\mathrm{ST}}^n(n = 0)$ versus V for the typical case ($\Delta_s > 0$), where $\theta_\alpha = 65^\circ$, $\theta_\beta = 50.55^\circ$,$w_0 = 0.40$, $G = 5000\mathrm{K/m}$.

From Figure 4, we have obtained the stable growth region of the SCN-DC rod eutectic, which is close to the experimental data for the steady growth of the SCN-DC rod eutectic [25]; for example, when $V = 3 \times 10^{-8}\mathrm{m/s}$ and $\varepsilon < \varepsilon_{\mathrm{ST}}^0 = 0.001716$, we say that the rod eutectic growth is stable. Next, we combined the obtained $\varepsilon_{\mathrm{ST}}^0$ with $\lambda_* = 2R = 2\varepsilon\kappa_D/V$ and predicted the relationship between the critical stable eutectic spacing of the material (SCN-DC) and the velocity under the conditions that the velocity V is greater than $3 \times 10^{-8}\mathrm{m/s}$ and where $G = 5000\mathrm{K/m}$ in, then compared it with the theoretical values predicted by J–H [25] and some experimental data [25]; the results are shown in Figure 5.

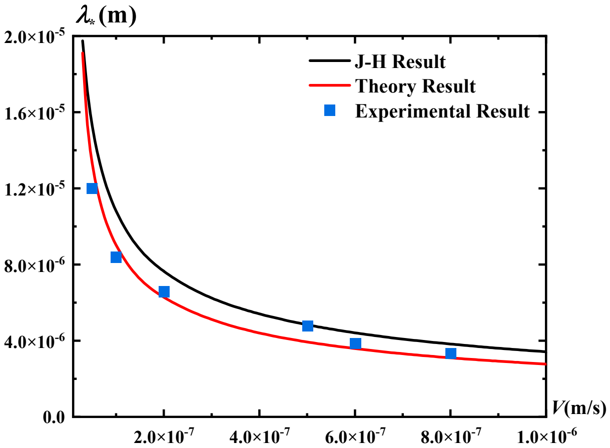

Figure 5. The critical eutectic spacing of λ_* with the speeding velocity V: λ_* and λ_*^{JH} as a function of V, where $w_0 = 0.40$, $G = 5000\mathrm{K/m}$.

It can be seen from the above Figure 5 that the predicted critical stable rod eutectic spacing in the case of $V > 3 \times 10^{-8}\mathrm{m/s}$, $G = 5000\mathrm{K/m}$ is smaller than the theoretical values predicted by J–H, and we found that the experimental data are close to the values we predicted and that when the velocity increases from $3 \times 10^{-8}\mathrm{m/s}$ to $3 \times 10^{-7}\mathrm{m/s}$, λ_*/λ_*^{JH} decreases from 0.968 to 0.819; when the velocity is greater than $3 \times 10^{-7}\mathrm{m/s}$, λ_*/λ_*^{JH} is close to the constant 0.811.

Additionally, we obtained the relationship between the critical small parameter, the critical eutectic spacing and the temperature gradient by changing the value of the temperature gradient, as shown in Figure 6:

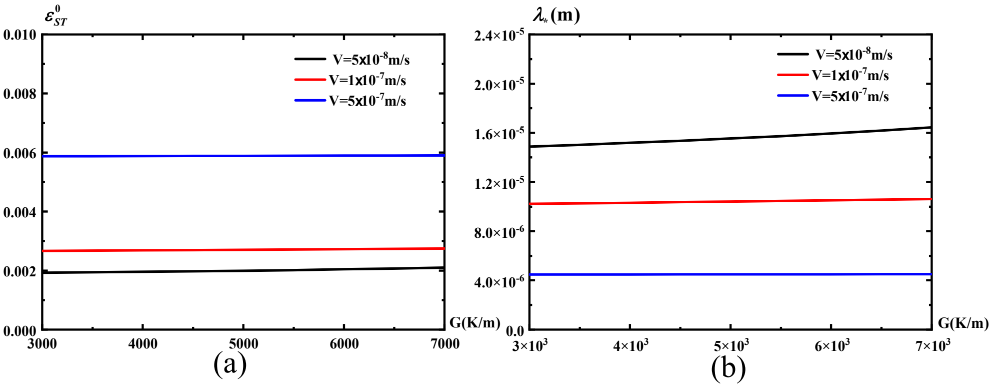

Figure 6. (**a**) The curves of the critical numbers of $\varepsilon^n_{\mathrm{ST}}(n = 0)$ of versus G for the typical case $(\Delta_s > 0)$; (**b**) the critical eutectic spacing of λ_* with the temperature gradient G, where $\theta_\alpha = 65^\circ$, $\theta_\beta = 50.55^\circ$,$w_0 = 0.40$.

It can be seen from Figure 6 that the critical small parameter and the critical eutectic spacing are less affected by the temperature gradient where $\theta_\alpha = 65^\circ$, $\theta_\beta = 50.55^\circ$,$w_0 = 0.40$. Only when the velocity is relatively small, that is, when $\Delta_s \to 0$ or $\Delta_s \sim O(1)$, the critical small parameter and the critical eutectic spacing are slightly affected by the temperature gradient and increase with the increase in the temperature gradient, but their changes are not obvious. When the velocity is relatively large, that is, when $\Delta_s \gg 1$, the critical parameters and the critical eutectic spacing almost do not change with the change in the temperature gradient.

6. Conclusions

In this paper, the linear instability mechanism of rod eutectic growth is studied. We performed the asymptotic analysis for the perturbations around the basic steady state of the rod eutectic system and obtained the global modes solution by solving the related eigenvalue problem. We obtain the analytic form of the global mode solution and the corresponding quantization conditions and predict the corresponding critical eutectic spacing. We find that the system allows for the real spectrum of the eigenvalue σ_0, and we find that there is a stable growth mode, the ST mode, for rod eutectic growth; when $\varepsilon < \varepsilon^0_{\mathrm{ST}}$, the rod eutectic growth is stable, when $\varepsilon > \varepsilon^0_{\mathrm{ST}}$, the rod eutectic growth is unstable and when $\varepsilon = \varepsilon^0_{\mathrm{ST}}$, the rod eutectic growth is of a neutral stability. Additionally, the critical eutectic spacing of SCN-DC predicted by us is smaller than that predicted by Jackson–Hunt, which is consistent with the corresponding experimental data. Finally, we found that the critical eutectic spacing and the stable region of rod eutectic growth changed little with the temperature gradient. Based on the content explored in this paper, we can better understand the growth of the rod-shaped eutectic; therefore, a foundation for the analytical study of rod eutectic oscillation growth has thus been laid.

Author Contributions: Conceptualization, X.L. and Y.G.; methodology, X.L.; validation, X.L. and Y.G.; formal analysis, X.L. and Y.G.; resources, X.L.; writing—original draft preparation, X.L. and Y.G.; writ-ing—review and editing, X.L.; supervision, X.L.; project administration, X.L.; funding ac-quisition, X.L. All authors have read and agreed to the published version of the manuscript.

Funding: This research was funded by National Natural Science Foundation of China (No.51961018). The APC was funded by National Natural Science Foundation of China (No.51961018).

Data Availability Statement: The data is confidential and inconvenient to publish.

Acknowledgments: The authors deeply grateful to the National Natural Science Foundation of China (No.51961018).

Conflicts of Interest: The authors declare no conflict of interest.

References

1. Xu, J.-J.; Li, X.-M.; Chen, Y.-Q. Global steady state solutions for lamellar eutectic growth in directional solidification. *J. Cryst. Growth* **2014**, *401*, 93–98. [CrossRef]
2. Chen, Y.-J.; Davis, S. Instability of triple junctions in lamellar eutectic growth. *Acta Mater.* **2001**, *49*, 1363–1372. [CrossRef]
3. Zhang, A.; Guo, Z.; Xiong, S.-M. Quantitative phase-field lattice-Boltzmann study of lamellar eutectic growth under natural convection. *Phys. Rev. E* **2018**, *97*, 053302. [CrossRef] [PubMed]
4. Akamatsu, S.; Bottin-Rousseau, S.; Şerefoğlu, M.; Faivre, G. A theory of thin lamellar eutectic growth with anisotropic interphase boundaries. *Acta Mater.* **2012**, *60*, 3199–3205. [CrossRef]
5. Akamatsu, S.; Bottin-Rousseau, S.; Faivre, G. Determination of the Jackson–Hunt constants of the In–In2Bi eutectic alloy based on in situ observation of its solidification dynamics. *Acta Mater.* **2011**, *59*, 7586–7591. [CrossRef]
6. Faivre, G.; Bottin-Rousseau, S.; Akamatsu, S. The trajectory of subboundary grooves during directional solidification of dilute alloys. *Comptes Rendus Phys.* **2013**, *14*, 149–155. [CrossRef]
7. Wang, W.-M.; Liu, J.-M.; Pan, X.; Liu, Z. Monte-Carlo simulation of regular lamellar eutectic growth in binary systems. *Mater. Sci. Eng. A* **2002**, *336*, 129–134. [CrossRef]
8. Xu, J.; Zhang, T.; Galenko, P.K. Rod eutectic growth in bulk undercooled melts. *Math. Methods Appl. Sci.* **2021**, *45*, 8022–8031. [CrossRef]
9. Meng, G.-H.; Lin, X.; Huang, W.-D. Interlamellar spacing and average interface undercooling of irregular eutectic in steady-state growth. *Trans. Nonferrous Met. Soc. China* **2008**, *18*, 405–409. [CrossRef]
10. Nestler, B.; Wheeler, A. A multi-phase-field model of eutectic and peritectic alloys: Numerical simulation of growth structures. *Phys. D Nonlinear Phenom.* **2000**, *138*, 114–133. [CrossRef]
11. Wang, L.; Lin, X.; Wang, M.; Huang, W. Solid–liquid interfacial energy and its anisotropy measurement from double grain boundary grooves. *Scr. Mater.* **2013**, *69*, 1–4. [CrossRef]
12. Xu, J.-J.; Chen, Y.-Q.; Li, X.-M. Global instabilities of lamellar eutectic growth in directional solidification. *J. Cryst. Growth* **2014**, *401*, 99–105. [CrossRef]
13. Lei, W.; Cao, Y.; Xin, L.; Kun, C.; Huang, W. Globular to lamellar transition during anomalous eutectic growth. *Model. Simul. Mater. Sci. Eng.* **2020**, *28*, 065014. [CrossRef]
14. Tu, Z.; Zhou, J.; Tong, L.; Guo, Z. A phase-field study of lamellar eutectic growth with solid-solid boundary anisotropy. *J. Cryst. Growth* **2019**, *532*, 125439. [CrossRef]
15. Akamatsu, S.; Bottin-Rousseau, S. Numerical Simulations of Locked Lamellar Eutectic Growth Patterns. *Metall. Mater. Trans. A* **2021**, *52*, 4533–4545. [CrossRef]

16. Zhang, A.; Guo, Z.; Jiang, B.; Song, J.; Pan, F.; Xiong, S. Effect of laser shock on lamellar eutectic growth: A phase-field study. *Int. J. Heat Mass Transf.* **2021**, *52*, 4533–4545. [CrossRef]
17. Sullivan, E.; Tomko, J.; Skelton, J.; Fitz-Gerald, J.; Hopkins, P.; Floro, J. Lamellar instabilities during scanning laser melting of Al–Cu eutectic and hypoeutectic thin films. *J. Alloy. Compd.* **2021**, *865*, 158800. [CrossRef]
18. Pusztai, T.; Rátkai, L.; Horváth, L.; Gránásy, L. Phase-field modelling of directional melting of lamellar and rod eutectic structures. *Acta Mater.* **2022**, *227*, 117678. [CrossRef]
19. Legese, S.S.; Olu, F.E. A Review of Lamellar Eutectic Morphologies for Enhancing Thermoelectric and Mechanical Performance of Thermoelectric Materials. *J. Indian Inst. Sci.* **2022**, *102*, 237–279. [CrossRef]
20. Liu, S.; Lee, J.; Trivedi, R. Dynamic effects in the lamellar–rod eutectic transition. *Acta Mater.* **2011**, *59*, 3102–3115. [CrossRef]
21. Teng, J.; Liu, S.; Trivedi, R. Growth and morphology of rod eutectics. *Acta Mater.* **2008**, *56*, 2819–2833. [CrossRef]
22. Şerefoğlu, M.; Napolitano, R.E.; Plapp, M. Phase-field investigation of rod eutectic morphologies under geometrical confinement. *Phys. Rev. E* **2011**, *84*, 011614. [CrossRef]
23. Parisi, A.; Plapp, M. Defects and multistability in eutectic solidification patterns. *Europhys. Lett.* **2010**, *90*, 26010. [CrossRef]
24. Akamatsu, S.; Bottin-Rousseau, S.; Perrut, M.; Faivre, G.; Witusiewicz, V.; Sturz, L. Real-time study of thin and bulk eutectic growth in succinonitrile–(d)camphor alloys. *J. Cryst. Growth* **2007**, *299*, 418–428. [CrossRef]
25. Serefoglu, M.; Napolitano, R. On the selection of rod-type eutectic morphologies: Geometrical constraint and array orientation. *Acta Mater.* **2008**, *56*, 3862–3873. [CrossRef]
26. Şerefoğlu, M.; Bottin-Rousseau, S.; Akamatsu, S.; Faivre, G.; Kaya, M.S. Dynamics of rod eutectic growth patterns in confined geometry. *IOP Conf. Ser. Mater. Sci. Eng.* **2012**, *27*, 012030. [CrossRef]
27. Perrut, M.; Akamatsu, S.; Bottin-Rousseau, S.; Faivre, G. Long-time dynamics of the directional solidification of rodlike eutectics. *Phys. Rev. E* **2009**, *79*, 032602. [CrossRef]
28. Basit, S.; Birinci, S.; Maraşlı, N. Growth of rod structure with static electrical field in the Al–Ni eutectic system. *J. Mater. Sci. Mater. Electron.* **2020**, *31*, 14055–14068. [CrossRef]
29. Galenko, P.K.; Xu, J. Rapid eutectic growth: From rod growth to diffusionless solidification. *Philos. Trans. R. Soc. A Math. Phys. Eng. Sci.* **2022**, *380*, 20200305. [CrossRef]
30. Ludwig, A.; Leibbrandt, S. Generalised 'Jackson–Hunt' model for eutectic solidification at low and large Peclet numbers and any binary eutectic phase diagram. *Mater. Sci. Eng. A* **2004**, *375*, 540–546. [CrossRef]
31. Meng, G.; Xie, H.; Lin, X. Estimation of rod-like phase spacing in melt-grown eutectic composites. *Sci. China Technol. Sci.* **2014**, *57*, 1794–1801. [CrossRef]
32. Trivedi, R.; Wang, N. Theory of rod eutectic growth under far-from-equilibrium conditions: Nanoscale spacing and transition to glass. *Acta Mater.* **2012**, *60*, 3140–3152. [CrossRef]
33. Li, X.-M.; Xu, F. Uniformly valid asymptotic solutions of rod eutectic growth in directional solidification for contact angles being the normal order. *J. Cryst. Growth* **2017**, *468*, 945–949. [CrossRef]
34. Bottin-Rousseau, S.; Witusiewicz, V.T.; Hecht, U.; Fernandez, J.; Laveron-Simavilla, A.; Akamatsu, S. Coexistence of rod-like and lamellar eutectic growth patterns. *Scr. Mater.* **2021**, *207*, 114314. [CrossRef]
35. Şerefoğlu, M.; Bottin-Rousseau, S.; Akamatsu, S. Lamella-rod pattern transition and confinement effects during eutectic growth. *Acta Mater.* **2022**, *242*, 118425. [CrossRef]
36. Kellner, M.; Kunz, W.; Steinmetz, P.; Hötzer, J.; Nestler, B. Phase-field study of dynamic velocity variations during directional solidification of eutectic NiAl-34Cr. *Comput. Mater. Sci.* **2018**, *145*, 291–305. [CrossRef]
37. Hassan, N.; Minakshi, M.; Ruprecht, J.; Liew, W.Y.H.; Jiang, Z.T. A Binary Salt Mixture LiCl-LiOH for Thermal Energy Storage. *Materials* **2023**, *16*, 1434. [CrossRef]
38. Baral, A.; Das, D.P.; Minakshi, M.; Ghosh, M.K.; Padhi, D.K. Probing Environmental Remediation of RhB Organic Dye Using α-MnO_2 under Visible- Light Irradiation: Structural, Photocatalytic and Mineralization Studies. *ChemistrySelect* **2016**, *1*, 4277–4285. [CrossRef]
39. Wu, R.Z.; Yan, Y.D.; Wang, G.X.; Murr, L.E.; Han, W.; Zhang, Z.W.; Zhang, M.L. Recent progress in magnesium-lithium alloys. *Int. Mater. Rev.* **2015**, *60*, 65. [CrossRef]
40. Dong, H.; Wang, L.; Liu, K.; Wang, L.; Jiang, B.; Pan, F. Microstructure and deformation behaviors of two Mg-Li dual-phase alloys with an increasing tensile speed. *Mater. Des.* **2016**, *90*, 157.
41. Mahmudi, R.; Shalbafi, M.; Karami, M.; Geranmayeh, A. Effect of Li content on the indentation creep characteristics of cast Mg–Li–Zn alloys. *Mater. Des.* **2015**, *75*, 184–190. [CrossRef]
42. Qu, Z.; Wu, L.; Wu, R.; Zhang, J.; Zhang, M.; Liu, B. Microstructures and tensile properties of hot extruded Mg-5Li-3Al-2Zn-xRE (rare earths) alloys. *Mater. Des.* **2014**, *54*, 792. [CrossRef]
43. Zhu, T.; Cui, C.; Zhang, T.; Wu, R.; Betsofen, S.; Leng, Z.; Zhang, J.; Zhang, M. Influence of the combined addition of Y and Nd on the microstructure and mechanical properties of Mg–Li alloy. *Mater. Des.* **2014**, *57*, 245. [CrossRef]
44. Wang, T.; Zhu, T.; Wu, R.; Miao, W.; Zhang, J.; Zhang, M. Microstructure and mechanical properties of LA51 and LA51-0.5Y alloys with different accumulated strains and rolling temperatures. *Mater. Des.* **2015**, *85*, 190. [CrossRef]
45. Karami, M.; Mahmudi, R. Orientation-dependent microstructure and shear flow behavior of extruded Mg–Li–Zn alloys. *Mater. Sci. Eng. A* **2015**, *636*, 493–501. [CrossRef]

46. Chen, D.; Jin, N.; Chen, W.; Wang, L.; Zhao, S.; Luo, D. Corrosion resistance of Ni/Cu/Ni-P triple-layered coating on Mg-Li alloy. *Surf. Coat. Technol.* **2014**, *254*, 440. [CrossRef]
47. Xu, J.-J. Interfacial wave theory of solidification: Dendritic pattern formation and selection of growth velocity. *J. Phys. Rev. A* **1991**, *43*, 930.